Journal of Luminescence 228 (2020) 117605

Contents lists available at ScienceDirect

Journal of Luminescence

journal homepage: http://www.elsevier.com/locate/jlumin

pH induced size tuning of $Gd_2Hf_2O_7:Eu^{3+}$ nanoparticles and its effect on their UV and X-ray excited luminescence

Santosh K. Gupta [a], Mitzy A. Penilla Garcia [b], Jose P. Zuniga [b], Yuanbing Mao [c,*]

[a] Radiochemistry Division, Bhabha Atomic Research Centre, Trombay, Mumbai, 400085, India
[b] Department of Chemistry, University of Texas Rio Grande Valley, 1201 West University Drive, Edinburg, TX, 78539, USA
[c] Department of Chemistry, Illinois Institute of Technology, 3105 South Dearborn Street, Chicago, IL, 60616, USA

ARTICLE INFO

Keywords:
$Gd_2Hf_2O_7$
Eu^{3+}
Nanoparticle
pH
Luminescence

ABSTRACT

Size tunable nanoparticles (NPs) have played an important role in areas of optoelectronics, drug delivery, magnetism and many others. Moreover, designing size-tunable NPs without exposing them to high temperature and long time thermal treatment is highly desirable to make agglomerate- and defect-free NPs. In this work, we have designed $Gd_2Hf_2O_7:Eu^{3+}$ (GHOE) NPs using the molten-salt synthesis (MSS) method with the precursors made from varying precipitant concentrations (correspondingly the pH of the precipitating solution). The obtained NPs have a decreasing size as the pH of the precipitating solution rises and a defect fluorite structure with a large fraction of Eu^{3+} ions localized at GdO_8 distorted scalenohedra, a small fraction residing at Hf^{4+} site, and the presence of oxygen vacacnies in the vicinity of $Eu_{Hf}^{\cdot}$. Maximum photoluminescence and radioluminescence outputs and internal quantum yield have been observed from the GHOE NPs made from 5.0% NH_4OH as precipitant due to optimum balance of surface defects and particle clustering. Judd-Ofelt analysis has confirmed that these GHOE NPs have lowest non-radiative transition probability, brightest red emission, largest branching ratio, and highest radiative transition rate. With increasing pH of the precipitating solution, the group symmetry of Eu^{3+} ions in the GHOE host decreases systematically from $D_4 \rightarrow C_{4v} \rightarrow C_{3v}$ and then saturates, consistent with the pH dependent asymmetry ratio value. Also, the extent of polarizability enhances and the Eu–O bond becomes more covalent as confirmed by the monotonic increase of Ω_2/Ω_4 ratio. Our work on these optical materials will assist the scientific community to make size-tunable nanoparticles at low synthesis temperature for efficient luminescent devices.

1. Introduction

Nanomaterials have at least one dimension falling in the size range of 1–100 nm [1]. Their catalytic, thermal, optical, magnetic, biological, mechanical, and chemical properties are dictated mainly by atomic physics rather than classical physics, which govern bulk materials [2,3]. Because of their unique properties [4,5], nanomaterials have inspired intense scientific curiosity and various technological applications. They have played essential roles in improving the living standards of human beings by virtue of several applications in the areas of catalysis, light emitting devices, sensing, scintillators, magnetism, bioimaging, persistence luminescence, medical, optoelectronics, etc. [6–18].

Synthesis methods play a huge role in designing well-defined nanomaterials with uniform and monodisperse morphology [19]. Recently it was found that the size of nanoparticles (NPs) plays a vital role in dictating their stability and various biological and physicochemical properties [20–23]. Particularly, in the area of luminescent NPs, their size is of utmost importance as they control defect density, amount of aggregation, surface texture, surface roughness, etc. [23], which indirectly influence their luminescence properties. In this sense, designing size tunable luminescent NPs will be interesting to investigate and harness their full potentials. In most of the reports, size variation is mostly induced by annealing them at high temperatures or exposing them at the same temperature for a long duration. These practices have several disadvantages as they may lead to the formation of large aggregates, which may cause light scattering and reduce the quantum efficiency of luminescent NPs.

Among several methods reported for synthesizing NPs, molten-salt synthesis (MSS) is one of the preferable routes owing to its advantages such as low formation temperature, scalability, environmentally

* Corresponding author.
E-mail address: ymao17@iit.edu (Y. Mao).

https://doi.org/10.1016/j.jlumin.2020.117605
Received 19 April 2020; Received in revised form 13 August 2020; Accepted 16 August 2020
Available online 14 September 2020

beingness, easy to operate, etc. [25] One of our recent MSS processes involves two steps: (i) co-precipitation to form complexed single-source precursors of all composing cations and (ii) thermal treatment of the precursors in molten salts to form desirable NPs. Based on our early experience, we found that the pH of the co-precipitation solution in the first step is critical in optimizing the size of the NPs with relatively low aggregations [17,24,26,27].

Most of our previous work was focused on f^0 types of pyrochlore hosts with a general formula of $A_2M_2O_7$, such as $La_2Hf_2O_7$ and $La_2Zr_2O_7$ consisting of La^{3+} as the A-site cation. Based on a plethora of work carried out by several researchers and by our group, we found that $Gd_2Hf_2O_7$ (GHO) type pyrochlore belongs to a very interesting class as they are located at the boundary of fluorite-pyrochlore boundary depicting several interesting properties. This includes high dielectric constant *k*, high thermal stability, and high melting point which impart them with several applications for magnetism, high *k* materials, scintillators, thermal barrier coatings, luminescence host, etc. [28–35] In fact, we have explored both lanthanide (Eu^{3+}) and actinide (U^{6+}) doped GHO NPs with an objective to understand the thermally induced phase transition, its effect on photo- and radio-luminescence, and their potential as nuclear waste host [33–35]. However, no studies have been reported on synthesizing size-tunable $Gd_2Hf_2O_7$:Eu^{3+} (GHOE) NPs by varying the concentration of precipitant (NH_4OH), in other words, the co-precipitating pH, in first step of the MSS method. Therefore, it will be interesting to explore the effect of pH induced size changes of the GHOE NPs on their crystal structure, UV excited luminescence, and X-ray excited luminescence. Study on UV excited state luminescence and X-rays excited luminescence will provide new opportunity to design novel size-tunable phosphors and scintillators.

Hence, in this work, we have synthesized GHOE NPs using different co-precipitating pH values. The obtained GHOE NPs were characterized using X-ray diffraction (XRD), Fourier-transform infrared spectroscopy (FTIR), Raman spectroscopy, field emission scanning electron microscopy (FESEM), UV excited photoluminescence (PL), and X-ray excited radioluminescence (RL), and lifetime spectroscopy. Our work provides an opportunity to the optical community to design size-tunable nanophosphors with optimum PL emission output, decent RL output, excited state lifetime, and quantum efficiency. We have also carried out Judd-Ofelt analysis to decipher various photophysical parameters which provide information on radiative and non-radiative transition rates, branching ratios, and Judd-Ofelt parameters as a function of the co-precipitating pH of the GHOE NPs.

2. Experimental

2.1. Synthesis

All the materials for the synthesis of the GHOE NPs were bought from Sigma-Aldrich with a purity of >99.0%. The GHOE NPs were synthesized using a two-step MSS route. First, a complex single-source precursor was generated by dissolving stoichiometric amounts of gadolinium nitrate hexahydrate ($Gd(NO_3)_3{\cdot}6H_2O$), hafnium dichloride oxide octahydrate ($HfOCl_2{\cdot}8H_2O$), and europium nitrate hexahydrate ($Eu(NO_3)_3{\cdot}6H_2O$) in 200 mL of Millipore water at room temperature. The aqueous mixture of these cationic components was mixed for ~30 min under magnetic stirring. To fine-tune the particle size and enable the investigation of the effects of precipitation pH on the optoelectronic characteristics of the GHOE NPs, ammonium hydroxide solutions with several different concentrations (0.5%, 2.5%, 5.0%, 10.0%, and 15.0%) were prepared. Each ammonium hydroxide solution was titrated dropwise into an aqueous mixture of the cationic components under stirring for 2 h. Five different samples were generated where all stoichiometric ratios were kept the same with the only variable of the concentration of ammonium hydroxide solution to precipitate the complex single-source precursor ($Gd(OH)_3{\cdot}HfO(OH)_2{\cdot}nH_2O$). The pH value of each of the co-precipitating solutions was measured by a pH meter. The relationship between the pH value of the co-precipitating solution and the concentration of the added ammonium hydroxide solution was plotted and shown in Fig. 1a. The second step is to form the GHOE NPs by thermal treatment of the co-precipitated complex single-source precursors in a molten salt under the same conditions. The MSS method has attracted a lot of attention recently to form complex metal oxides due to its simplicity and adaptable protocol. Specifically, the complex single-source precursors were mixed with potassium nitrate (KNO_3) and sodium nitrate ($NaNO_3$) at a molar ratio of 1:30:30 and grinded to fine powder mixtures. The resultants were placed in alumina crucibles and heated at 650 °C at a ramp rate of 1 °C·min^{-1} for 6 h. After the annealing period, the salts were washed off using DI water till the GHOE NPs were free from any residual salts. The final five samples were subject to full characterization in terms of their purity, shape, size, and optical performance. For simplicity, the samples are denoted as GHOE-0.5, GHOE-2.5, GHOE-5.0, GHOE-10.0, and GHOE-15.0 according to the concentrations of used ammonium hydroxide solutions.

2.2. Characterization

XRD data of the generated GHOE NPs were collected using a Bruker D8 X-ray diffractometer coupled with a Cu source K_a with a 0.15406 nm wavelength operating at 40 kV and 40 mA. The data was collected in a 2θ mode ranging from 10° to 90° with a step size of 0.04° at a rate of 2.0° per minute. Raman spectra were taken using a Bruker Senterra system using a 785 nm laser. The scans were set for a range of 80 cm^{-1} to 1530 cm^{-1} and ten accumulations. FTIR was conducted on a Thermo Nicolet Nexus 470 FT-IR system. The scans were taken in transmittance mode covering a wide range from 100 cm^{-1} to 4000 cm^{-1}. SEM images were collected using a Carl Zeiss sigma VP field emission instrument operating at 5 kV. PL and RL data were collected using an FLS 980 (Edinburg Instruments) coupled with both a continuous and a pulse Xenon lamps. The instrument was modified for RL experiments using an Ag source with 0.52 Å wavelength operating at 60 kV and 200 mA.

3. Results and discussion

3.1. XRD, FTIR and Raman spectra

The GHOE NPs were subjected to structural characterization using XRD, FTIR, and Raman spectroscopy to ensure their quality. The reflected XRD peaks are well defined, sharp, and with high intensity (Fig. 1b). The nature of the peaks indicates that the GHOE NPs are highly crystalline and have a relatively small crystalline size.

The nanocrystallite size of all the samples was further estimated by the Debye Scherer formula coupled with the Williamson-Hall approach to account for lattice strain broadening. The crystallite size estimated from peak broadening and strain in all the samples is given in Table 1.

It is clearly seen from this table that the crystallite size decreases with increasing co-precipitating pH. The same has been ascribed to the fact that increasing NH_4OH concentration gives more single-source precursor ($Gd(OH)_3{\cdot}HfO(OH)_2{\cdot}nH_2O$) nucleii. This eventually leads to the reduction of the particle size of the amorphous single-source precursor which give smaller sized GHOE NPs [36]. The reduction in crystallite size with the increase of co-precipitation pH was also observed from the synthesis of zinc oxide and lutetium oxide NPs [37,38].

The reflection planes from the XRD patterns show a defect fluorite structure ($Fm\bar{3}m$ space group) since there are no superlattice peaks (2-theta = 29°, 37°) that would correspond to its pyrochlore counterpart ($Fd\bar{3}m$ space group). In previous work, we highlighted the importance of annealing temperature for generating pyrochlore structures [33]. We focus on the effects of precipitating pH in this work. There is no evidence of structural selection by just adjusting the co-precipitation pH at the co-precipitation stage during the formation of the complex single-source precursor. These two almost identical structural phases are relatively

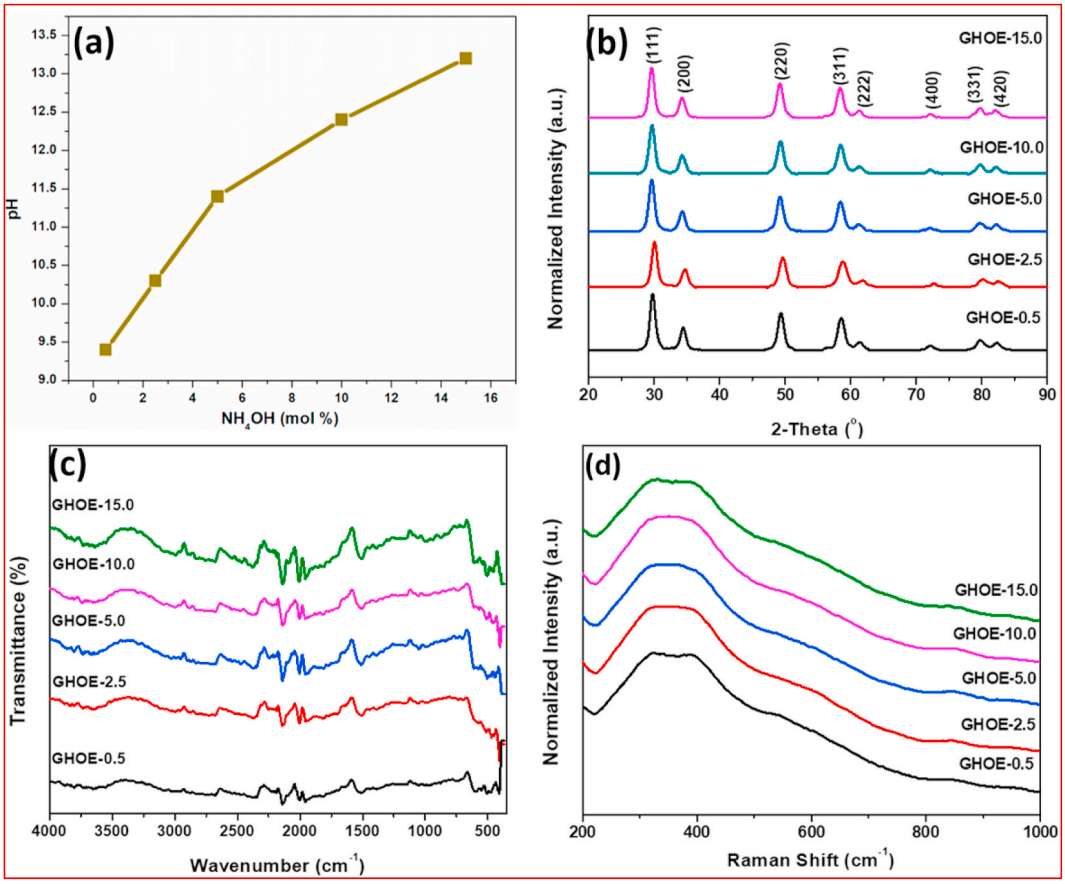

Fig. 1. (a) The relationship between the pH value of the co-precipitating solution and the concentration of the added ammonium hydroxide solution, (b) XRD patterns, (c) FTIR spectra, and (d) Raman spectra of the GHOE NPs.

Table 1
The calculated strain and crystallite size of the GHOE NPs synthesized with different co-precipitation pH values.

Samples	2θ (°)	FWHM (radians)	Strain (ϵ) (× 10^{-3})	Crystalline size (nm)
GHOE-0.5	29.80	0.81	2.61 ± 0.97	19.3 ± 5.9
GHOE-2.5	30.08	0.83	2.57 ± 1.5	18.0 ± 7.9
GHOE-5.0	29.65	0.86	2.75 ± 1.3	15.4 ± 5.1
GHOE-10.0	29.70	0.88	1.70 ± 1.2	13.0 ± 3.2
GHOE-15.0	29.64	0.91	1.34 ± 0.67	12.9 ± 1.8

difficult to distinguish by lab-scale x-ray diffractometer due to their cubic nature. It requires additional quality check-up to fully understand the crystal phase of the synthesized GHOE NPs.

FTIR spectra (Fig. 1c) were taken to explore the purity and composition of the GHOE NPs. In addition, FTIR can probe metal-oxygen vibrations making it an essential tool to examine local disorder. The broad band in the region of 3070–3590 cm^{-1} present in all of the FTIR spectra was ascribed to N–H or O–H stretching vibrations, which might come from the used precipitant NH_4OH and water molecules present in the complex single-source precursor or from adsorbed moisture after the final synthesis [39]. Here, the intensity of the OH vibration at 3500 cm^{-1} increments with increasing precipitant NH_4OH concentration confirming higher OH presence on the surface of the GHOE NPs. More OH vibration could cause nonradiative pathways dissipating the photon count and reducing luminescence intensity as discussed below. The IR peaks located in the range of 1300–1600 cm^{-1} are due to the bending vibration of O–H bond [40]. The IR absorption band at 700-900 cm^{-1} is attributed to the wagging vibration of N–H band. The characteristic pyrochlore peak of the GHO is located at 500 cm^{-1} [41].

Raman spectroscopy was carried to identify the actual structure of GHOE. Based on the theory of point group, the ordered pyrochlore (OP) structure of $A_2B_2O_7$ composition shows chracteristics 6 closely spaced peaks in the range of 200–1000 cm^{-1}, which are attributed to $\Gamma_{pyr} = A_{1g} + E_g + 4F_{2g}$ [7,24,26]. On the other hand, disordered fluorite (DF) phase typically shows a single broad peak due to $\Gamma_{flu} = F_{2g}$ owing to the random distribution of oxygen ions over eight available positions, which cause large structural disordering. Regarding the ionic radius ratio r_A/r_B as a critical parameter in deciding the structure of pyrochlore lattice, it is reported that the disordered fluorite phase is favored when r_A/r_B is less than 1.46 whereas the ordered pyrochlore phase is the prevalent structure when r_A/r_B is more than 1.46. Interestingly, r_{Gd}/r_{Hf} is equal to ~1.48 for GHO as the host of the GHOE NPs, which is slightly greater than 1.46. Thus, the availability of these GHOE NPs offers a unique opportunity to study the DF to OP phase evolution as this can be induced thermodynamically which we have observed in our earlier work [33]. The DF structure will be shown by only vibrational mode in the range of ~300 cm^{-1} pertaining to the F_{2g} metal-oxygen vibrational mode while the OP phase will show six vibrational modes. Fig. 1d shows a single broad Raman peak that confirms the DF structure of our GHOE NPs, and therefore agrees with our XRD results.

3.2. SEM

SEM images (Fig. 2) were captured for the GHOE NPs to evaluate the effect of the co-precipitation pH on the particle size. The images show that most of the NPs are spherical in shape and some of them have clustered in larger particles with several small spheres. The shape seems

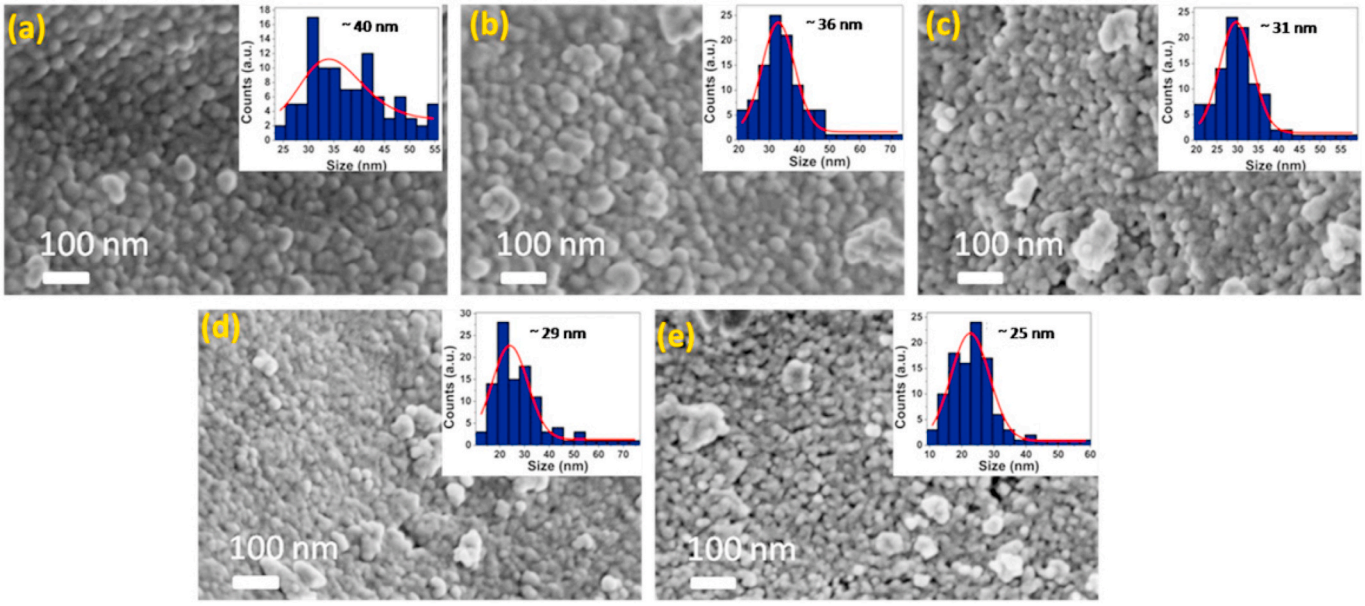

Fig. 2. SEM images of the GHOE NPs prepared with different co-precipitation pH. Insets show the histograms of particle size distribution using the ImageJ software.

to be unchanged by the manipulation of the co-precipitation pH was uses as a digital caliper to quantify the particle size for each sample. The histograms generated by ImageJ software for each sample give estimated average particle size of 40, 36, 31, 29, and 25 nm with increasing ammonium hydroxide concentration used for the co-precipitation. This suggests that the particle size of the GHOE NPs decreases with increasing co-precipitation pH, which agrees with the calculated particle size from our XRD results (Table 1 and Fig. 1b).

3.3. PL

Excitation spectra of the GHOE NPs (Fig. 3a) consists of two main features. One broad band peaks around 270 nm due to the $O^{2-} \rightarrow Eu^{3+}$ charge transfer band (CTB) and some fine small peaks encompass in this CTB at around 300–325 nm due to several defects present in the GHO host as reported in our earlier work [33]. Several peaks in the range of 350–500 nm are ascribed to intra-configuration f-f bands of Eu^{3+} ions. The two most important peaks are located at 395 nm due to the $^7F_0 \rightarrow {}^5L_6$ transition and at 465 nm due to the $^7F_0 \rightarrow {}^5D_2$ transition. The intensity of the CTB is much more than that of the intra-configuration f-f

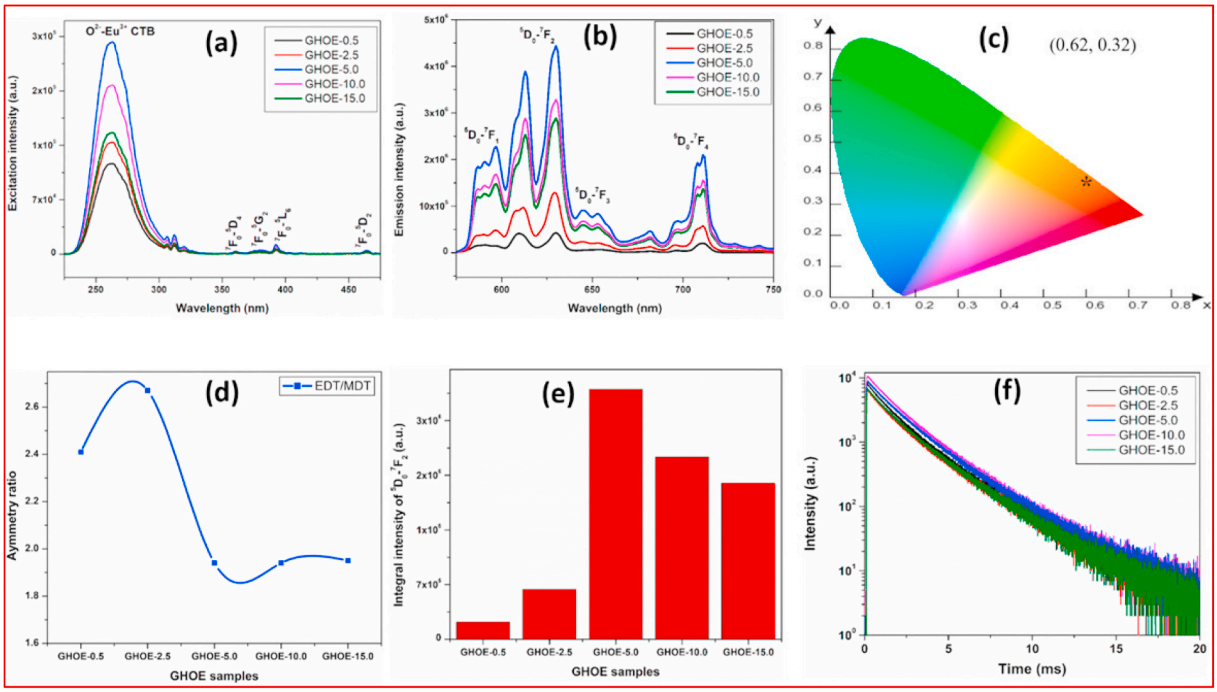

Fig. 3. (a) Excitation spectra (λ_{em} = 615 nm) and (b) emission spectra (λ_{ex} = 270 nm) of the GHOE NPs. (c) Color coordinate diagram of the GHOE-5.0 NPs. (d) Variation of asymmetry ratio *vs.* the co-precipiation pH, (e) the variation of integral PL intensity *vs.* the co-precipitation pH, and (f) luminescence decay profiles of the GHOE NPs.

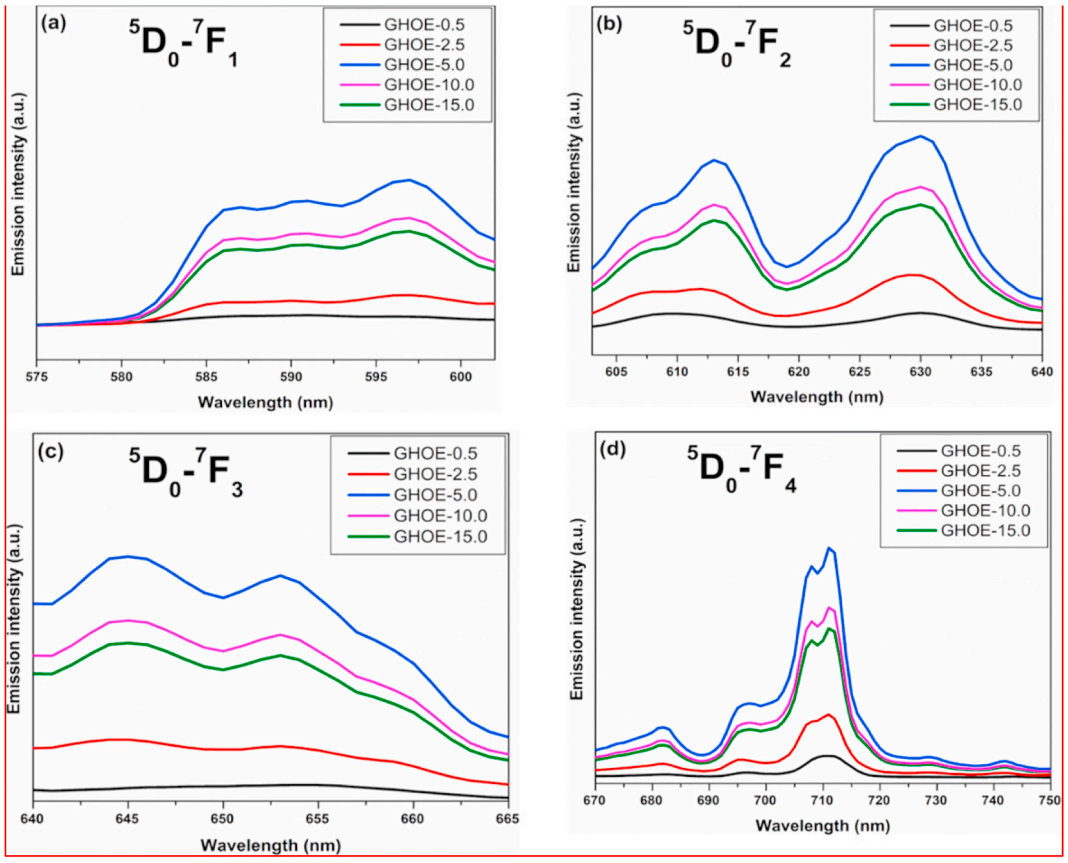

Fig. 4. Stark splitting of various transitions of Eu^{3+} from our GHOE NPs: (a) $^5D_0 \rightarrow {}^7F_1$, (b) $^5D_0 \rightarrow {}^7F_2$, (c) $^5D_0 \rightarrow {}^7F_3$, and (d) $^5D_0 \rightarrow {}^7F_4$.

Table 2
Stark splitting components of various transitions of the GHOE NPs.

Samples	$^5D_0 \rightarrow {}^7F_1$	$^5D_0 \rightarrow {}^7F_2$	$^5D_0 \rightarrow {}^7F_3$	$^5D_0 \rightarrow {}^7F_4$	Point group symmetry [42]
GHOE-0.5	1	2	1	3	D_4
GHOE-2.5	2	2	2	4	C_{4v}
GHOE-5.0	3	3	3	5	C_{3v}
GHOE-10.0	3	3	3	5	C_{3v}
GHOE-15.0	3	3	3	5	C_{3v}

bands suggesting luminescence in the GHOE NPs is governed by host to dopant energy transfer.

The emission spectra of the GHOE NPs (Fig. 3b) is rich in Eu^{3+} characteristic peaks located at 592, 619, 650 and 710 nm due to $^5D_0 \rightarrow {}^7F_1$, $^5D_0 \rightarrow {}^7F_2$, $^5D_0 \rightarrow {}^7F_3$, and $^5D_0 \rightarrow {}^7F_4$ transitions, respectively. Among these transitions, $^5D_0 \rightarrow {}^7F_1$ is allowed by magnetic dipole transition (MDT, $\Delta J = \pm 1$) and is not affected much by the local field and environment of Eu^{3+} dopants. Its corresponding transition peak is intense wherein europium is localized in symmetric environment. On the other hand, $^5D_0 \rightarrow {}^7F_2$ is allowed by forced electric dipole transition (EDT, $\Delta J = \pm 2$) and is strongly affected by the local field and environment of Eu^{3+} ions. Its corresponding transition is intense wherein Eu^{3+} is localized in asymmetric environment without center of inversion. $^5D_0 \rightarrow {}^7F_3$ is neither allowed by EDT nor by MDT. $^5D_0 \rightarrow {}^7F_4$ is ascribed to EDT. In our emission spectra, the intensity of EDT is much higher than that of MDT suggesting that Eu^{3+} ions are localized in highly asymmetric environment in all of the GHOE samples which lacks of inversion symmetry. Color coordinates were also calculated for one of the representative sample GHOE-5.0. Its values fall in the region showing bright red emission (Fig. 3c).

One informative parameter is the asymmetry ratio ($A_{21} = I_{EDT}/I_{MDT}$). It is > 1.0 for all of the samples (Fig. 3d), which further suggest low symmetry around Eu^{3+} ions in the GHO lattice. In fact, the A_{21} value increases initially with increasing co-precipitation pH values. At pH = 11.4 (GHOE-5.0) and beyond, it saturated around 11.95 (Note: the curve connecting the data points does not have real scientific meaning and is for the purpose of guiding the eyes). There are two cationic sites in GHO: 8-coordinated GHO_8 scalenohedra which is highly distorted and HfO_6 octahedra which is relatively more ordered. Based on closeness in ionic radius, a large fraction of Eu^{3+} ions preferably goes to the Gd^{3+} site compared to Hf^{4+} site, which invokes the need of charge compensation by oxygen vacancies. Here, the high intensity of the $^5D_0 \rightarrow {}^7F_2$ transition is clearly justified by the fact that a large fraction of Eu^{3+} ions occupies the distorted GdO_8 scalenohedra. Meanwhile, the presence of MDT $^5D_0 \rightarrow {}^7F_1$ in the emission spectra indicates that a decent amount of Eu^{3+} ions does occupy highly symmetric HfO_6. The Eu^{3+} ions occupying Hf^{4+} sites may lead to the generation of negative antisite defects (Eu'_{Hf}) and positive oxygen vacancy defects ($V_{\ddot{O}}$) as indicated below by the Kroger-Vink notation:

$$Eu^{3+} + Hf^{4+} Eu'_{Hf} + V_{\ddot{O}} \quad (1)$$

Moreover, the PL emission intensity increases with increasing co-precipitation pH up to that for the GHOE-5.0 NPs, and there was a reduction of the PL emission intensity beyond that (Fig. 3e). There are two factors to be considered for this trend: surface defect density (SDD) and degree of clustering (DOC). The initial rise of the PL emission intensity is because the DOC predominates over SDD initially with increasing co-precipiation pH (up to 11.4). Lower the DOC, smaller the scattering of excitation and emission photon, and higher the PL emission intensity. Beyond the co-precipitation pH of 11.4, the SDD overpowers the DOC as the particle size of the GHOE NPs keeps decreasing (from 39

nm to 25 nm as tabulated in Table 1) with increasing co-precipitation pH. Surface defects are known to provide alternative pathways to non-radiative transitions and hence the observed reduction of the PL emission intensity when the co-precipitation pH further increased from 11.4 to 13.2.

The luminescence decay profiles of the GHOE NPs (Fig. 3f) can be fitted using the biexponential equation:

$$I(t) = A_1 \exp(-t/t_1) + A_2 \exp(-t/t_2) \quad (2)$$

The fitted two lifetime values do not change much and are in the ranges of 650–700 μs (t_1, 72%) and 1.45–1.60 ms (t_2, 28%). The short lifetime (t_1) is ascribed to Eu^{3+} ions sitting at asymmetric GdO_8 scalenohedra. This is in line with phonon-energy concept according to which f-f transitions are LaPorte relaxed at asymmetric center and are forbidden in case of symmetric centers. Accordingly, the long lifetime (t_2) value is ascribed to Eu^{3+} ion sitting at symmetric HfO_6 octahedra. The fractional distribution of these two lifetimes is also in line with the observed PL emission spectra with more intense EDT peak compared to MDT peak (Fig. 3b), i.e. a large fraction of Eu^{3+} ions is at asymmetric site compared to at symmetric site. Lifetime data throw similar light with 72% Eu^{3+} ions occupying the GdO_8 and 28% occupying the HfO_6.

We have further studied the effect of the co-precipitation pH on Stark splitting of the PL spectra of the GHOE NPs. Stark splitting occurs with the $^5D_0 \rightarrow {}^7F_J$ (J = 1, 2, 3, and 4) transition of Eu^{3+} (Fig. 4 & Table 2) due to electric field effect of the crystalline $Gd_2Hf_2O_7$ host. From Table 2, the point group symmetry changes from D_4 to C_{4v} to C_{3v}, and then there is saturation at the GHOE-5.0 NPs and beyond. This observation is completely in line with our A_{21} plot (Fig. 3d) wherein the A_{21} values do not change for the samples of the GHOE-5.0, GHOE-10.0, and GHOE-15.0 NPs. This suggests that the Eu^{3+} environment attain more or less constancy in the GHOE NPs prepared at high co-precipitation pH. Moreover, as the concentration of the precipitant NH_4OH increased from 0.5 to 5.0%, the point group symmetry of Eu^{3+} changes from D_4 to C_{3v}, which suggests that Eu^{3+} becomes more asymmetric and reaches the maxima at the co-precipitation concentration of 5.0%. This is one of the reasons for the highest PL emission intensity observed from the GHOE-5.0 NPs.

3.4. Judd-Ofelt (JO) analysis

By taking into consideration of the refractive index of the GHO host, the calculated lifetime, the integral peak area of the corrected PL spectra, we employed several equations for the GHOE NPs to calculate various photophysical parameters, such as A_R, A_{NR}, IQE, JO parameter, and branching ratio, which are listed in Table 3 [43,44].

From the literature, it is well-known that the short range JO parameter, Ω_2, is an indication of the covalency and polarizability of Eu–O bond, and the long range JO parameter, Ω_4, is related to viscosity and rigidity which are the bulk properties of phosphor hosts. High Ω_2 values point to high covalent and polarizable environments around Eu^{3+} ions in hosts. For all of our GHOE NP samples, the Ω_2 parameter is larger compared to the Ω_4 value, which can be ascribed to asymmetric environment and polarizable Eu–O bond. The extent of polarizability enhances and the Eu–O bond becomes more covalent as the co-precipiation pH is raised for synthesizing these GHOE NPs, which is further confirmed by the monotonic increase of Ω_2/Ω_4. The radiative transition rate A_R and non-radiative transition rate A_{NR} maximizes and minimizes, respectively at the co-precipitation NH_4OH concentration of 5.0%. This is attributed to optimum SDD and DOC of the GHOE-5.0 NPs compared to other GHOE samples. Internal quantum efficiency (IQY) value also increases with increasing co-precipiation pH up to that for the GHOE-5.0 NPs. This is attributed to highest A_R and lowest A_{NR} values from the GHOE-5.0 NPs. There is complete agreement with the trend of PL emission intensity (Fig. 3e) and IQY value. The purity of red emission is governed by the branching ratio values β_s (s = 1, 2, and 4). It is clearly seen that the β_2 value is much larger than the β_1 and β_4 values. This suggests that most of the photon output results in red emission and orange and near infrared emissions are low from the GHOE NPs.

3.5. RL

Scintillating phosphors convert high-energy photons (γ-rays and x-rays) into tens of thousands of low energy photons mostly in the visible range. RL emission spectra of the GHOE NPs excited by X-ray (Fig. 5a) are characterized by four distinct bands located at 596, 615, 650, and 711 nm corresponding to the $^5D_0 \rightarrow {}^7F_1$, $^5D_0 \rightarrow {}^7F_2$, $^5D_0 \rightarrow {}^7F_3$, and $^5D_0 \rightarrow {}^7F_4$ transitions of Eu^{3+} ions, respectively. The RL emission spectra of the GHOE NPs are very similar to their PL emission spectra (Fig. 3a) while the PL spectra demonstrate relatively more splitting at high co-precipitation pH and the RL spectra show constant extent of splitting. This can be attributed to different energies of the excitations used: x-ray *vs.* UV light at 270 nm. UV excitation proceeds by host sensitization whereas x-ray excitation processes through photoelectric effect and the creation of excitons.

The variation of integrated RL intensity of the 615 nm peak corresponding to $^5D_0 \rightarrow {}^7F_2$ transition as a function of the precipitant NH_4OH concentration used to synthesizing these GHOE NPs (Fig. 5b) shows that the maximum RL output is achieved with the NH_4OH concentration of 5.0%, which is consistent withthe PL results (Fig. 3e). Emission intensity of phosphors is strongly affected by surface defects present on nanomaterials. There are two affecting parameters for luminescence properties: surface defects and agglomeration. Surface defects provide non-radiative pathways whereas agglomeration scatters incident and emitted light. Hence, the increase of both parameters reduces PL and RL intensity. Our SEM images and XRD data show that there is gradual decrease of particle size from 39 nm to 25 nm with increasing NH_4OH concentration from 0.5 to 15.0%. The initial increase of RL intensity with increasing NH_4OH concentration from 0.5 to 5.0% is attributed to reduced light scattering. Beyond that, the effect of surface defect dominates the quenching of the RL.

The process of converting x-ray excitation into visible light by scintillators is usually divided into four different steps as pictorially represented in Fig. 6 [45,46]. The nature of heavier constituents is very important for efficient x-ray scintillation process because x-ray absorption intensity varies proportionally to Z_{eff}^4/AE [3] where Z_{eff} and A are effective atomic number and atomic mass, respectively, and E is the energy of x-ray [47]. Accordingly, GHO is a desirable host for x-ray scintillators due to its high effective atomic number of Hf (72) and density (7.9 g/cc).

In the first step, a scintillating material absorbs x-ray through photoelectric effect (PE), which creates electrons and holes. At the beginning, the x-ray (E < few 100 KeV) interacts with Hf atom of the

Table 3
Various photophysical parameters of the GHOE NPs synthesized with different co-precipitation pH values.

[NH_4OH] (%)	A_R (s^{-1})	A_{NR} (s^{-1})	IQY (%)	Ω_2 (*10^{-20})	Ω_4 (*10^{-20})	β_1 (%)	β_2 (%)	β_4 (%)	Ω_2/Ω_4
0.5	268	234.19	52.9	0.48	0.298	19	60.2	18.6	1.61
2.5	265	211.86	55.5	0.485	0.299	18.9	60.5	18.5	1.62
5.0	314	187.71	64.2	0.488	0.297	18.8	60.6	18.3	1.64
10.0	285	204.49	61.9	0.498	0.304	18.5	60.9	18.4	1.68
15.0	271	210.52	59.3	0.503	0.313	18.3	60.8	18.7	1.72

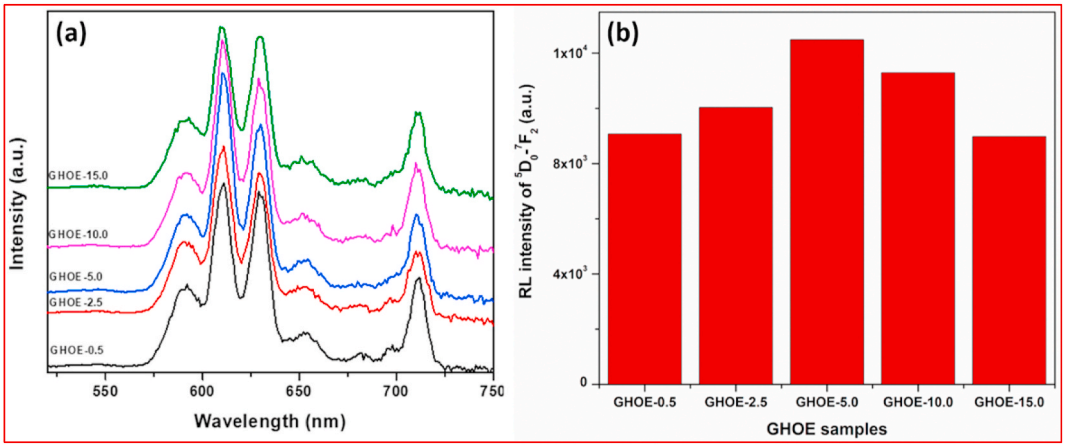

Fig. 5. (a) RL emission spectra under x-ray excitation and (b) the variation of integral RL intensity of the GHOE NPs.

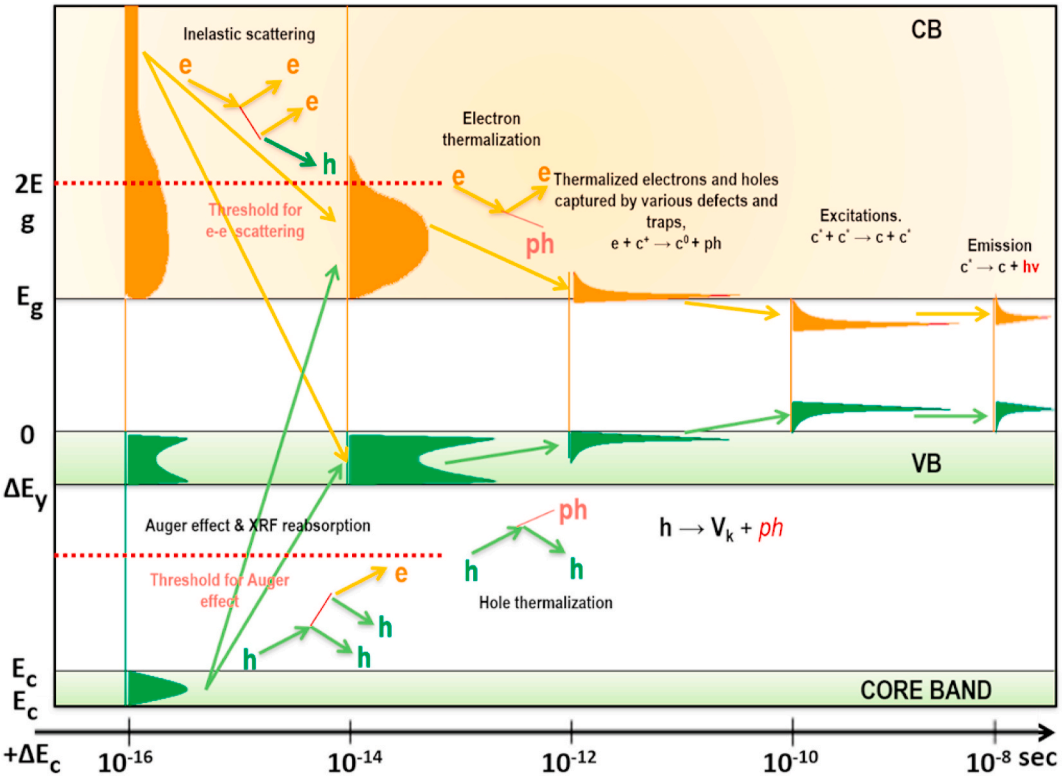

Fig. 6. Proposed scintillation mechanism of the GHOE NPs [50].

pyrochlore GHOE NPs mostly through PE. Similar interaction mechanism was predominant in $CsPbBr_3$ nanocrystals where x-ray interacts with Pb atom of the perovskite nanocrystals through PE [45]. In the second step, the electrons and holes relax to generate large number of secondary electrons, holes, photons, and plasmons. Such relaxation also induces several other electronic excitations. These secondary electrons and holes lose their energy via electron-phonon interaction to give electron-hole pairs with near band gap energy. The third stage involves the transport of the electron-hole pairs (excitons) through the scintillating material to luminescent centers (traps), i.e. the excitation of the luminescent centers. The final stage is the resulting luminescence. A scintillating material which has a high light output and short lifetime under photoexcitation may have a very low light output and/or long lifetime under x-ray excitation [48]. This is due to the energy losses and delays in the energy migration processes which are absent in PL where the luminescent centers are directly and intentionally excited [49]. This mechanism has been described in great details by Lecoq et al. [50] Here we have only discussed the process happens when electrons get excited and go from valence (VB) to conduction band (CB) whereas there are many processes happening in the core band.

4. Conclusion

In this work, pure GHOE NPs with different sizes were synthesized using the MSS method by varying the pH of the precipitating solution, which is achieved by varying the concentration of NH_4OH precipitant. The formed spherical NPs with a defect fluorite structure have a narrowing size from 39 to 25 nm when the pH increases from 9.4 to 13.2. The GHOE NPs synthesized with 5.0% NH_4OH at pH 11.4 have the maximum luminescence emission intensity and internal quantum yield

due to the optimum balance of surface defects, degree of aggregation, and non-radiative channels. Asymmetry ratio analysis suggests that the Eu^{3+} dopant lacks inversion symmetry in the GHO host with a large fraction located at GdO_8 scalenohedra and others at Hf^{4+} sites. In line with asymmetry ratio values, Stark splitting analysis shows that the point group symmetry of Eu^{3+} changes from $D_4 \rightarrow C_{4v} \rightarrow C_{3v}$ as the precipitating pH increases from 9.4 to 11.4 and then saturates in the pH range of 11.4–13.2. The Judd-Ofelt analysis shows an increase of polarizability and covalency of the Eu–O bond as the pH of the precipitating solution raises. Such a complete spectrum of work wherein size tunable NPs are synthesized just by varying the precipitating pH and its effect on the photoluminescence and radioluminescence properties gives a new dimension in the areas of nanophoshors for solid-state lighting and scintillator applications.

Credit author statement

Santosh K. Gupta: Conceptualization, Data Curation, Formal analysis, Visualization, Writing. **M.A.P. Garcia:** Data Curation, Methodology, Investigation. **Jose P. Zuniga:** Data Curation, Methodology, Investigation. **Yuanbing Mao:** Conceptualization, Supervision, Visualization, Writing - Review & Editing.

Declaration of competing interest

The authors declare that they have no known competing financial interests or personal relationships that could have appeared to influence the work reported in this paper.

Acknowledgement

YM thanks the financial support by the National Science Foundation under CHE (award # 1952803 and 1710160) and the IIT startup funds. SKG thanks the United States-India Education Foundation (USIEF, India) and the Institute of International Education (IIE, USA) for his Fulbright Nehru Postdoctoral Fellowship (Award# 2268/FNPDR/2017).

References

[1] H. Xin, B. Namgung, L.P. Lee, Nanoplasmonic optical antennas for life sciences and medicine, Nature Reviews Materials 3 (2018) 228–243.
[2] Q.A. Akkerman, G. Rainò, M.V. Kovalenko, L. Manna, Genesis, challenges and opportunities for colloidal lead halide perovskite nanocrystals, Nat. Mater. 17 (2018) 394–405.
[3] T.E. Long, C.B. Williams, Printing nanomaterials in shrinking gels, Science 362 (2018) 1244–1245.
[4] X. Chen, S.S. Mao, Titanium dioxide nanomaterials: synthesis, properties, modifications, and applications, Chem. Rev. 107 (2007) 2891–2959.
[5] A. Taloni, M. Vodret, G. Constantini, S. Zapperi, Size effects on the fracture of microscale and nanoscale materials, Nature Review Materials 3 (2018) 211–224.
[6] B. Srivastava, S.K. Gupta, Y. Mao, Bright persistent green emitting water-dispersible Zn_2GeO_4:Mn nanorods, Dalton Trans. 49 (2020) 7328–7340.
[7] S.K. Gupta, J.P. Zuniga, M. Abdou, M. Thomas, B.S. Guiton, Y. Mao, Lanthanides doped lanthanum hafnate as multicolored phosphors for warm white lighting and scintillators, Chem. Eng. J. 379 (2020) 122314.
[8] C. Hernandez, S.K. Gupta, J.P. Zuniga, J. Vidal, R. Galvan, M. Martinez, H. Guzman, L. Chavez, Y. Mao, K. Lozano, Performance evaluation of Ce^{3+} doped flexible PVDF fibers for efficient optical pressure sensors, Sensor. Actuator. B Chem. 298 (2019) 111595.
[9] B. Srivastava, S.K. Gupta, Y. Mao, Remarkable Enhancement of photoluminescence and persistent luminescence of NIR emitting $ZnGa_2O_4$:Cr^{3+} nanoparticles, CrystEngComm. 22 (2020) 2491–2501.
[10] M. Valdez, S.K. Gupta, K. Lozano, Y. Mao, ForceSpun polydiacetylene nanofibers as colorimetric sensor for food spoilage detection, Sensor. Actuator. B Chem. 297 (2019) 126734.
[11] O.S. Kwon, H.S. Song, T.H. Park, J. Jang, Conducting nanomaterial sensor using natural receptors, Chem. Rev. 119 (2019) 36–93.
[12] U. Prasad, J. Prakash, S.K. Gupta, J.P. Zuniga, Y. Mao, B. Azeredo, A.M. Kannan, Enhanced photoelectrochemical water splitting with Er and W co-doped bismuth vanadate with WO_3 heterojunction based 2-dimensional photoelectrode, ACS Appl. Mater. Interfaces 11 (2019) 19029–19039.
[13] A.R. Chowdhury, A.M. Abdullah, I. Hussain, J. Lopez, D. Cantu, S. K Gupta, Y. Mao, S. Danti, J. Uddin, Lithium doped zinc oxide based flexible piezoelectric-triboelectric hybrid nanogenerator, Nanomater. Energy 61 (2019) 327–336.
[14] B. Srivastava, S.K. Gupta, Y. Mao, Singular red emission from upconverting $ZnGa_2O_4$:Yb,Er nanoparticles co-doped by Cr^{3+}, J. Mater. Chem. C 8 (2020) 6370–6379.
[15] V. Yadav, S. Roy, P. Singh, Z. Khan, A. Jaiswal, 2D MoS_2-based nanomaterials for therapeutic, bioimaging, and biosensing applications, Small 15 (2019) 1803706.
[16] R. Mani, S.K. Gupta, P.S. Ghosh, H. Jiang, Yellow emission from low coordination site of Sr_2SiO_4:Eu^{2+},Ce^{3+}: influence of lanthanide dopants on the electron density and crystallinity in crystal site engineering approach, Chem. Eur J. 24 (2018) 1–12.
[17] S.K. Gupta, J.P. Zuniga, P.S. Ghosh, M. Abdou, Y. Mao Correlating, Structure and luminescence properties of undoped and Eu^{3+} doped $La_2Hf_2O_7$ nanoparticles prepared with different coprecipitating pH values through experimental and theoretical studies, Inorg. Chem. 57 (2018) 11815–11830.
[18] B. Yao, J. Zhang, X. Fan, J. He, Y. Li, Surface engineering of nanomaterials for photo-electrochemical water splitting, Small 15 (2019) 1803746.
[19] J.A. Darr, J. Zhang, N.M. Makwana, X. Weng, Continuous hydrothermal synthesis of inorganic nanoparticles: applications and future directions, Chem. Rev. 117 (2017) 11125–11238.
[20] M.J. Mulvihill, S.E. Habas, I.J. Plante, J. Wan, T. Mokari, Influence of size, shape, and surface coating on the stability of aqueous suspensions of CdSe nanoparticles, Chem. Mater. 22 (18) (2010) 5251–5257.
[21] J.L.R. Lopez, J.M.M. Carrizales, J.P.P. Baez, H. Barron, Size effect and shape stability of Nanoparticles, Key Eng. Mater. 444 (2010) 47–68.
[22] A. Albanese, P.S. Tang, W.C.W. Chan, The effect of nanoparticle size, shape, and surface chemistry on biological systems, Annu. Rev. Biomed. Eng. 14 (2012) 1–16.
[23] M.A. Gatoo, S. Naseem, M.Y. Arfat, A.M. Dar, K. Qasim, Physicochemical properties of nanomaterials: implication in associated toxic manifestations, Biomed. Res. Int., Article ID 498420 (2012) 8.
[24] J.P. Zuniga, S.K. Gupta, M. Abdou, H.A. De Santiago, A.A. Puretzky, M.P. Thomas, B.S. Guiton, J. Liu, Y. Mao, Size, structure and luminescence of $Nd_2Zr_2O_7$ nanoparticles by molten salt synthesis, J. Mater. Sci. 54 (2019) 12411–12423.
[25] M.A.P. Garcia, S.K. Gupta, Y. Mao, Effects of molten-salt processing parameters on the structural and optical properties of preformed $La_2Zr_2O_7$:Eu^{3+} nanoparticles, Ceram. Int. 46 (2020) 1352–1361.
[26] S.K. Gupta, M. Abdou, J.P. Zuniga, P.S. Ghosh, E. Molina, B. Xu, Y. Mao, Roles of oxygen vacancies and pH induced size changes on photo- and radioluminescence of undoped and Eu^{3+}-doped $La_2Zr_2O_7$ nanoparticles, J. Lumin. 209 (2019) 309–315.
[27] M. Pokhrel, M.G. Brik, Y. Mao, Particle size and crystal phase dependent photoluminescence of $La_2Zr_2O_7$:Eu^{3+} nanoparticles, J. Am. Ceram. Soc. 98 (2015) 3192–3201.
[28] A.M. Durand, P. Klavins, L. Corruccini, Heat capacity of the frustrated magnetic pyrochlores $Gd_2Zr_2O_7$ and $Gd_2Hf_2O_7$, J. Phys. Condens. Matter 20 (2008) 235208.
[29] A. Ali Biswas, Y. Jana, Study on the low-temperature properties of pyrochlores $Gd_2Hf_2O_7$ and $Gd_2Zr_2O_7$, using crystal-field theory, AIP Conference Proceedings, AIP 1349 (2011) 1121–1122.
[30] S. Kumar, H. Gupta, First principles study of dielectric and vibrational properties of pyrochlore hafnates, Solid State Sci. 14 (2012) 1405–1411.
[31] N. Cepeda-Sánchez, A. Fuentes, F. López-Cota, M. Rodríguez-Reyes, J. Díaz-Guillén, Mechanochemical synthesis and electrical properties of $Gd_2Hf_{2-x}Zr_xO_7$ solid electrolytes for their use in SOFC's, J. Appl. Electrochem. 45 (2015) 1231–1237.
[32] V.G. Sevastyanov, E.P. Simonenko, N.P. Simonenko, V.L. Stolyarova, S.I. Lopatin, N.T. Kuznetsov, Synthesis, vaporization and thermodynamic properties of superfine $Nd_2Hf_2O_7$ and $Gd_2Hf_2O_7$, Eur. J. Inorg. Chem. 2013 (2013) 4636–4644.
[33] S.K. Gupta, M. Abdou, J.P. Zuniga, P.S. Ghosh, Y. Mao, Thermally induced disorder–order phase transition of $Gd_2Hf_2O_7$:Eu^{3+} nanoparticles and its implication on photo- and radioluminescence, ACS Omega 4 (2019) 2779–2791.
[34] M. Abdou, S.K. Gupta, J.P. Zuniga, Y. Mao, Insight into the effect of A-site cations on structural and optical properties of $RE_2Hf_2O_7$:U nanoparticles, J. Lumin. 209 (2019) 425–434.
[35] M. Pokhrel, K. Wahid, Y. Mao, Systematic studies on $RE_2Hf_2O_7$:5%Eu^{3+} (RE = Y, La, Pr, Gd, Er, and Lu) nanoparticles: effects of the A-site RE^{3+} cation and calcination on structure and photoluminescence, J. Phys. Chem. C 120 (27) (2016) 14828–14839.
[36] M. Tsega, F. Dejene, Influence of acidic pH on the formulation of TiO_2 nanocrystalline powders with enhanced photoluminescence property, Heliyon 3 (2017), e00246.
[37] Y. Li, J. Zhang, X. Zhang, Y. Luo, X. Ren, H. Zhao, X. Wang, L. Sun, C. Yan, Near-infrared to visible upconversion in Er^{3+} and Yb^{3+} codoped Lu_2O_3 nanocrystals: enhanced red color upconversion and three-photon process in green color upconversion, J. Phys. Chem. C 113 (2009) 4413–4418.
[38] K. Swaroop, H. Somashekarappa, Effect of pH values on surface morphology and particle size variation in ZnO nanoparticles synthesised by co-precipitation method, Res. J. Recent Sci. 2277 (2015) 2502.
[39] M. Abu-Dalo, N. Al-Rawashdeh, I. Al-Mheidat, N. Nassory, Construction of uranyl selective electrode based on complex of uranyl ion with new ligand carboxybenzotriazole in PVC matrix membrane, IOP Conf. Ser. Mater. Sci. Eng. 92 (2020), 012023 (IOP Publishing).
[40] S.K. Gupta, J.P. Zuniga, M. Abdou, Y. Mao, Thermal annealing effects on $La_2Hf_2O_7$:Eu^{3+} nanoparticles: a curious case study of structural evolution and site-specific photo- and radio-luminescence, Inorg. Chem. Front. 5 (2018) 2508–2521.
[41] W.E. Klee, G. Weitz, Infrared spectra of ordered and disordered pyrochlore-type compounds in the series $RE_2Ti_2O_7$, $RE_2Zr_2O_7$ and $RE_2Hf_2O_7$, J. Inorg. Nucl. Chem. 31 (1969) 2367–2372.
[42] Q. Ju, Y. Liu, R. Li, L. Liu, W. Luo, X. Chen, Optical spectroscopy of Eu^{3+}-doped BaFCl nanocrystals, J. Phys. Chem. C 113 (2009) 2309–2315.

[43] M. Keskar, S.K. Gupta, R. Phatak, S. Kannan, V. Natarajan, Optical Properties of Eu^{3+} activated thorium molybdate and thorium tungstate: structure, local symmetry and photophysical properties, J. Photochem. Photobiol. Chem. 311 (2015) 59–67.
[44] S.K. Gupta, M. Mohapatra, V. Natarajan, S.V. Godbole, On the unusual photoluminescence of Eu^{3+} in α-$Zn_2P_2O_7$: a time resolved emission spectrometric and Judd-Ofelt study, RSC Adv. 3 (2013) 20046.
[45] Q. Chen, J. Wu, X. Ou, B. Huang, J. Almutlaq, A.A. Zhumekenov, X. Guan, S. Han, L. Liang, Z. Yi, J. Li, X. Xie, Y. Wang, Y. Li, D. Fan, D.B.L. Teh, A.H. All, O. F. Mohammed, O.M. Bakr, T. Wu, M. Bettinelli, H. Yang, W. Huang, X. Liu, All-inorganic perovskite nanocrystal scintillators, Nature 561 (7721) (2018) 88–93.
[46] P. Lecoq, M. Korzhik, A. Vasiliev, Can transient phenomena help improving time resolution in scintillators? IEEE Trans. Nucl. Sci. 61 (1) (2014) 229–234.
[47] M. Nikl, A. Yoshikawa, Recent R&D trends in inorganic single-crystal scintillator materials for radiation detection, Advanced Optical Materials 3 (4) (2015) 463–481.
[48] M. Nikl, Scintillation detectors for x-rays, Meas. Sci. Technol. 17 (4) (2006) R37.
[49] J.P. Zuniga, S.K. Gupta, M. Pokhrel, Y. Mao, Exploring optical properties of $La_2Hf_2O_7$:Pr^{3+} nanoparticles under UV and X-ray excitations for potential lighting and scintillating applications, New J. Chem. 42 (2018) 9381–9392.
[50] A. Vasil'ev, Relaxation of hot electronic excitations in scintillators: account for scattering, track effects, complicated electronic structure, in: Proc. of the Fifth Int. Conf. on Inorganic Scintillators and Their Applications, SCINT99Proc. of the Fifth Int. Conf. on Inorganic Scintillators and Their Applications, SCINT99, Moscow State University, Moscow, 2000, pp. 43–52.